JGR Space Physics

TECHNICAL REPORTS: METHODS
10.1029/2018JA026191

Derivation of Hemispheric Ionospheric Current Functions From Ground-Level Magnetic Fields

D. R. Weimer[1,2]

[1]Center for Space Science and Engineering Research, Virginia Tech, Blacksburg, VA, USA, [2]National Institute of Aerospace, Hampton, VA, USA

Key Points:
- Calculations of ionospheric equivalent current functions from ground-level magnetic field values are reviewed
- The vertical magnetic field is needed to derive the telluric currents, and effects of the ring current should be considered
- The telluric currents enhance the horizontal field and suppress the vertical component

Correspondence to:
D. R. Weimer,
dweimer@vt.edu

Citation:
Weimer, D. R. (2019). Derivation of hemispheric ionospheric current functions from ground-level magnetic fields. *Journal of Geophysical Research: Space Physics*, *124*, 3149–3161. https://doi.org/10.1029/2018JA026191

Received 11 OCT 2018
Accepted 17 MAR 2019
Accepted article online 5 APR 2019
Published online 16 APR 2019

Abstract The horizontal currents in the high-latitude ionosphere are the primary driver of the magnetic field perturbations that are observed at the surface of the Earth. These currents and their ground effects are an important aspect of the magnetosphere-ionosphere coupling process. This paper discusses the method of inversion that uses spherical harmonic potential function, in which magnetic field measurements on the ground can be used to derive maps of the "ionospheric equivalent currents," a mathematical representation of the horizontal currents flowing on a thin shell. It is shown that the use of both internal telluric and external current sources is required when fitting the spherical harmonic series; otherwise, the ionospheric currents will be overestimated. Furthermore, the inversion needs to compensate for magnetic effects of the magnetospheric ring current; otherwise, this current is projected onto the ionosphere. The amplification of the surface horizontal magnetic field and the suppression of the vertical magnetic field are demonstrated. The equivalent currents may be useful for estimating the ionospheric conductivity values. Additionally, these currents can be compared with the results from simulation models as a means of validation.

Plain Language Summary Currents in the high-latitude ionosphere produce changes in the magnetic field at the surface of the Earth. This paper discusses a technique that uses measurements of these changes in the magnetic field to solve the problem of deriving maps of the currents flowing in the ionosphere. While the first description of this method dates back to the 1940s, this obscure practice can now be more useful with the more recent availability of globally distributed magnetic field measurements. The details of this particular "inversion" technique are described. It is shown that for greatest accuracy, the mirror image currents that occur beneath the Earth's surface need to be considered, as well as the currents that are actually located in the magnetosphere, far above the ionosphere. This result is useful in the study of the interaction between the solar wind and the Earth's magnetosphere, and the resulting currents.

1. Introduction

The magnetic field variations at the surface of the Earth are caused mainly by external currents, which are driven by the forces of the solar wind and the embedded Interplanetary Magnetic Field (IMF) and their interaction with the Earth's dipolar magnetic field. Magnetic field measurements have served as diagnostic tool for observing this interaction, dating back to before the space age. One such method has been the calculation of the "current-function" (Chapman & Bartels, 1940), better known as the "ionospheric equivalent current function" (Kamide et al., 1981; Richmond & Kamide, 1988).

While the methods for deriving these current functions have been in existence for a while, in years past they were not often applied due to the difficulty in obtaining global-scale measurements of the magnetic fields for time periods of interest. With the advent of the internet-accessible database services such as SuperMag (Gjerloev, 2012), the derivation of the ionospheric currents may become more routine, as seen in recent papers (Laundal, Finlay, et al., 2016; Laundal, Gjerloev, et al., 2016; Pothier et al., 2015). Another use is described by Amm (2001) and demonstrated by Green et al. (2007), in which the current function can be combined with maps of the electric fields and field-aligned currents in order to derive the ionosphere conductivities, provided that the neutral wind in the ionosphere can be neglected (Amm, 1995). There is also a potential use of the equivalent current functions to help improve numerical models of the coupled solar wind-magnetosphere-ionosphere system. For example, a comparison of equivalent current maps with model outputs for similar conditions could help pinpoint where a model needs improvement.

One purpose of this paper is to describe how the current functions are derived and to make more accessible content found in previous, less known works. Additionally, while other papers have included some of the same formulas that are shown here, details have often been omitted, with the result that students and others may have trouble employing this technique. The results shown here were developed as part of a project, still in progress, to derive ionospheric conductivities; this paper is intended to provide the background material for later publications. Spherical harmonics are used in the method presented here. As discussed later in section 6, other methods exist for obtaining the ionospheric currents from a set of magnetic field measurements.

2. Derivation of the Magnetic Potential Function

The equivalent currents in the ionosphere can be derived from magnetic field values at the surface of the Earth by first fitting the measurements to a geomagnetic potential function on a spherical cap. It is assumed that the Earth's internal, dipole field has already been removed from the magnetic field measurements. This is usually done through baseline subtraction (Gjerloev, 2012; Weimer et al., 2010). The formulas shown here are basically identical to those presented by Haines (1988) and Haines and Torta (1994). As these publications are not well known, the essential equations are provided here.

These two previous works had described calculations that could be employed on a spherical cap having a "half-angle" of less than 90°, through the use of Spherical Cap Harmonic Analysis (Haines, 1985). This Spherical Cap Harmonic Analysis is based on Legendre functions $P^m_{n_k(m)}(\cos\theta)$ that have noninteger values of the degree $n_k(m)$, which vary with the "half angle" of the spherical cap, as well as the order m and integer, reference degree k (Haines, 1985). When the half angle of the spherical cap reaches 90°, then $n_k(m)$ becomes equal to the integer k and conventional Legendre polynomials can be used. As all of the examples shown here use data extending to the magnetic equator, all equations shown below are expressed in terms of Legendre polynomials, $P^m_k(\cos\theta)$, rather than the functions $P^m_{n_k(m)}(\cos\theta)$.

The geomagnetic potential function $V(r,\theta,\lambda)$ is expressed as a series of terms that include contributions from both external and internal currents:

$$V(r,\theta,\lambda) = a\sum_{k=0}^{K_i}\sum_{m=0}^{k}\left(\frac{a}{r}\right)^{k+1} P^m_k(\cos\theta)(g^{m,i}_k\cos m\lambda + h^{m,i}_k\sin m\lambda) + a\sum_{k=0}^{K_e}\sum_{m=0}^{k}\left(\frac{r}{a}\right)^{k} P^m_k(\cos\theta)(g^{m,e}_k\cos m\lambda + h^{m,e}_k\sin m\lambda). \quad (1)$$

This potential has units of Tesla meters, so that the spatial derivatives have units of Tesla. If the Legendre functions use Schmidt quasi-normalization, then the g and h coefficients have units of Tesla. The e superscripts refer to the external sources, the currents flowing above the surface of the Earth, while the i superscripts refer to the internal sources. In the application described here we are only concerned with the internal sources that are induced by the external, ionospheric currents. These telluric, image currents are separate from the dynamo currents that produce the Earth's main magnetic field, which is also modeled through the use of (1). The altitude and depth of these sources do not need to be known to obtain the solution. The K_i and K_e in (1) are the upper limits of the degree k in the summations. The symbol a represents a fixed, reference radius, usually taken to be the radius of the Earth.

If there are no local currents in the region where the magnetic field is being modeled, so that the curl of this field is zero, then the vector field $\mathbf{B}$ may be obtained from the gradient of the potential function:

$$\mathbf{B} = -\nabla V(r,\theta,\lambda). \quad (2)$$

In the application described here the values of $\mathbf{B}$ refer to the short-term, temporal perturbations in the magnetic field that are superposed on the Earth's main field due to geomagnetic disturbances.

As noted by Haines (1985), if the summations include only the terms that have odd values of $k - m$, then the value of all $P^m_k(\cos\theta)$, as well as the potential $V(r,\theta,\lambda)$, is zero at the half angle of the spherical cap, the low-latitude boundary. If only the terms are used that have even values of $k - m$, then the derivative of $P^m_k(\cos\theta)$ with respect to θ is zero at this boundary, and therefore, the northward component of $\mathbf{B}$ is also zero. In the examples shown here only the odd $k - m$ combinations are used. Both Friis-Christensen et al. (1985) and Laundal, Gjerloev, et al.,(2016) had also used the odd $k - m$ combination.

The values of the coefficients $g_k^{m,i}$, $h_k^{m,i}$, $g_k^{m,e}$, and $h_k^{m,e}$ are obtained through a least squares fit of the potential function $V(r, \theta, \lambda)$ to a set of magnetic field measurements, through (2). Notes about the fitting process are contained in the appendix. In order to compute this fit, it is necessary to expand (2) in terms of the spherical harmonic coefficients. From Haines (1988), the northward, eastward, and vertical (downward) components of the magnetic field are expressed as

$$B_N = \sum_{k=0}^{K_i}\sum_{m=0}^{k}\left(\frac{a}{r}\right)^{k+2}\frac{dP_k^m(\cos\theta)}{d\theta}(g_k^{m,i}\cos m\lambda + h_k^{m,i}\sin m\lambda) + \sum_{k=0}^{K_e}\sum_{m=0}^{k}\left(\frac{r}{a}\right)^{k-1}\frac{dP_k^m(\cos\theta)}{d\theta}(g_k^{m,e}\cos m\lambda + h_k^{m,e}\sin m\lambda), \tag{3}$$

$$B_E = \sum_{k=0}^{K_i}\sum_{m=0}^{k}\left(\frac{a}{r}\right)^{k+2}\frac{mP_k^m(\cos\theta)}{\sin\theta}(g_k^{m,i}\sin m\lambda - h_k^{m,i}\cos m\lambda) + \sum_{k=0}^{K_e}\sum_{m=0}^{k}\left(\frac{r}{a}\right)^{k-1}\frac{mP_k^m(\cos\theta)}{\sin\theta}(g_k^{m,e}\sin m\lambda - h_k^{m,e}\cos m\lambda), \tag{4}$$

$$B_V = -\sum_{k=0}^{K_i}\sum_{m=0}^{k}(k+1)\left(\frac{a}{r}\right)^{k+2}P_k^m(\cos\theta)(g_k^{m,i}\cos m\lambda + h_k^{m,i}\sin m\lambda) + \sum_{k=0}^{K_e}\sum_{m=0}^{k}(k)\left(\frac{r}{a}\right)^{k-1}P_k^m(\cos\theta)(g_k^{m,e}\cos m\lambda + h_k^{m,e}\sin m\lambda). \tag{5}$$

In order to demonstrate the use of these formulas, examples are shown from a set of simulated magnetic field values, which are obtained from the empirical model described by Weimer (2013). This model was constructed from ground-based magnetic field measurements obtained over an 8-year period. Data from 149 different locations in the Northern Hemisphere were used, although not all sites were operational during the entire 8-year period. Baseline values were subtracted from the measured values prior to their use in the model's construction. As described by Weimer et al. (2010), these baseline values varied over time, and the processing steps that were used depended on whether or not the magnetometers were permanent observatories, which measured the total magnetic field in geographic coordinates. The variometers, which sensed only the geomagnetic fluctuations, often reported their data in local magnetic coordinates, and sometimes these instruments were realigned during site visits for maintenance. Prior to the derivation of the empirical model, each measurement was translated and rotated from geographic coordinates to magnetic latitude and magnetic local time (MLT) coordinates. The modified apex coordinates described by Richmond (1995) were used for the transformations and based on the description of geomagnetic apex coordinates by VanZandt et al. (1972). In the collected data, the measurements that lie near a given latitude and local time may have originated from multiple geographic locations, at various dates and times.

In this empirical model each of the three vector components is calculated separately, each based on an independent spherical harmonic expansion that spans the northern, geomagnetic hemisphere. As described in more detail by Weimer (2013), the spherical harmonic coefficients are derived from functions of the model input parameters: the magnitude and orientation (clock angle) of the IMF in the *Y-Z* plane in Geocentric Solar Magnetic coordinates, the solar wind velocity, the dipole tilt angle (Hapgood, 1992, 1997), and the solar index $F_{10.7}$. The maximum degree used in the spherical harmonic expansion was 31, limited by latitudinal gaps in magnetometer locations. The maximum order m used in this model was 3, which has been found to be sufficient to resolve the typical electrodynamic patterns in the polar regions.

Figure 1 shows the three components of the magnetic field perturbations produced by this model with input values of 10 nT for the magnitude of the IMF in the Geocentric Solar Magnetic *Y-Z* plane, at a "clock angle" of 180° in this plane (southward). The value used for the solar wind velocity was 400 km/s, zero dipole tilt angle, and 120 sfu for the $F_{10.7}$. For purpose of this demonstration, the simulated measurements are distributed uniformly on the hemispherical cap at 0.5° latitude steps and 0.5-hr steps in MLT, or 7.5° longitude.

Note that the equations for the derivatives in (3)–(5) were originally applied by Haines and Torta (1994) to a case involving a set of magnetic field measurements in geographic coordinates, to get the equivalent

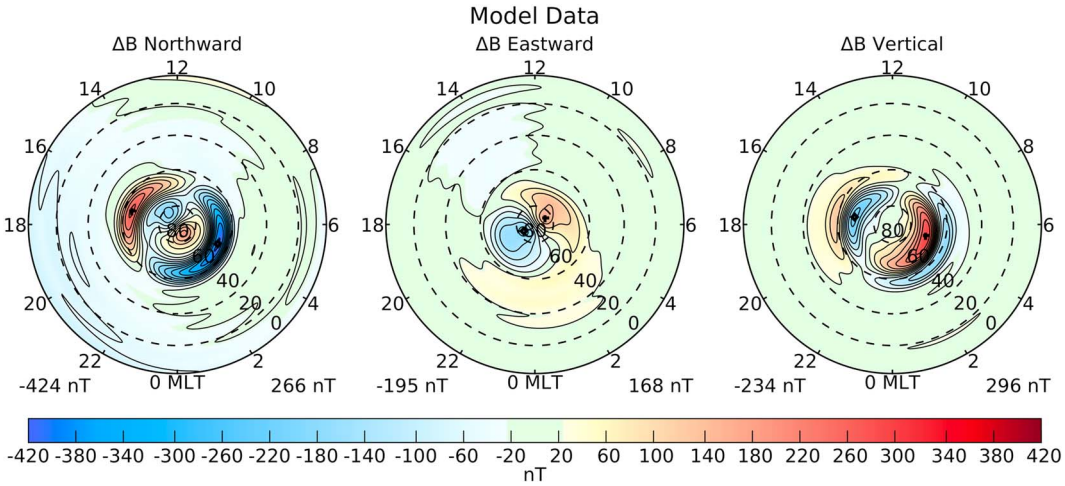

Figure 1. Example magnetic field values, shown in geomagnetic apex latitude and magnetic local time (MLT) coordinates. These three magnetic field components were produced by an empirical model for a 10-nT-southward interplanetary magnetic field, a solar wind velocity of 400 km/s, and zero dipole tilt angle.

current function that was also mapped in geographic coordinates. However, it is more complicated when going from geographic measurements to apex coordinates, as the lines of constant latitude and longitude in two coordinate systems are not exactly orthogonal to each other, as shown in the illustrations by Emmert et al. (2010) and Laundal and Richmond (2017). Therefore, when using measurements at various locations and times in geographic coordinates, then corrections should be applied to these derivatives in order to derive a magnetic potential function in magnetic apex coordinates (Laundal, Finlay, et al., 2016). As the outputs from the empirical model are already in magnetic apex coordinates, then equations (3)–(5) can be used as an approximation, treating the coordinates "as though they were true spherical coordinates, $\Delta B_{q\phi}$ and $\Delta B_{q\lambda}$ as though they were true magnetic components, and applying standard analysis techniques like spherical harmonic analysis" (Richmond, 1995).

Example results from fitting these simulated data with the potential function V, through the use of equations (1)–(5), are shown in Figure 2. The figure shows the values of the the northward, eastward, and vertical fields that are recalculated from the fitted potential, from (3)–(5). Even though the fitted data cover the entire hemisphere, in order to show more clearly the details within the auroral regions, these graphs only extend down to 50° latitude. To obtain the results shown in these graphs, the upper limits K_i and K_e for the degree k in equations (1) and (1)–(8) were both set to 34, while the upper limit for m in these equations was min(k,3). Through experimentation it was found that this value of the limiting degree (34) needed to be higher than what was used in the original model (31), contrary to expectations. To understand why, it is important to note that derivatives of a function are being fit to the original vector components and the relationships between the associated Legendre polynomials and their derivatives are nonlinear.

For purpose of demonstration, the top row in Figure 2 shows the result of a fit that only uses the terms for the external sources, ignoring the terms involving $g_k^{m,i}$ and $g_k^{m,i}$. This fit could use only the northward and eastward components of the simulated magnetic field. With the internal terms left out of (5), then the least-error fit solution fails if the vertical component is included. However, as shown in the top row in Figure 1, afterward, the vertical field can still be calculated from this solution for V. Not surprisingly, the results show that in this case the northward and eastward components derived from the fit match the simulated, model data reasonably well, while the vertical component does not match.

For the results shown in the middle row of Figure 2, the process was repeated, this time using the terms for both the internal and external sources, and including the vertical field values in the fitting process. In this case the vertical field that is derived from the potential function matches the simulated data very well, actually better than the other two components. Some differences from the simulated data can be expected, since the 2013 empirical model did not use a magnetic potential function but instead modeled each of the three vector components separately.

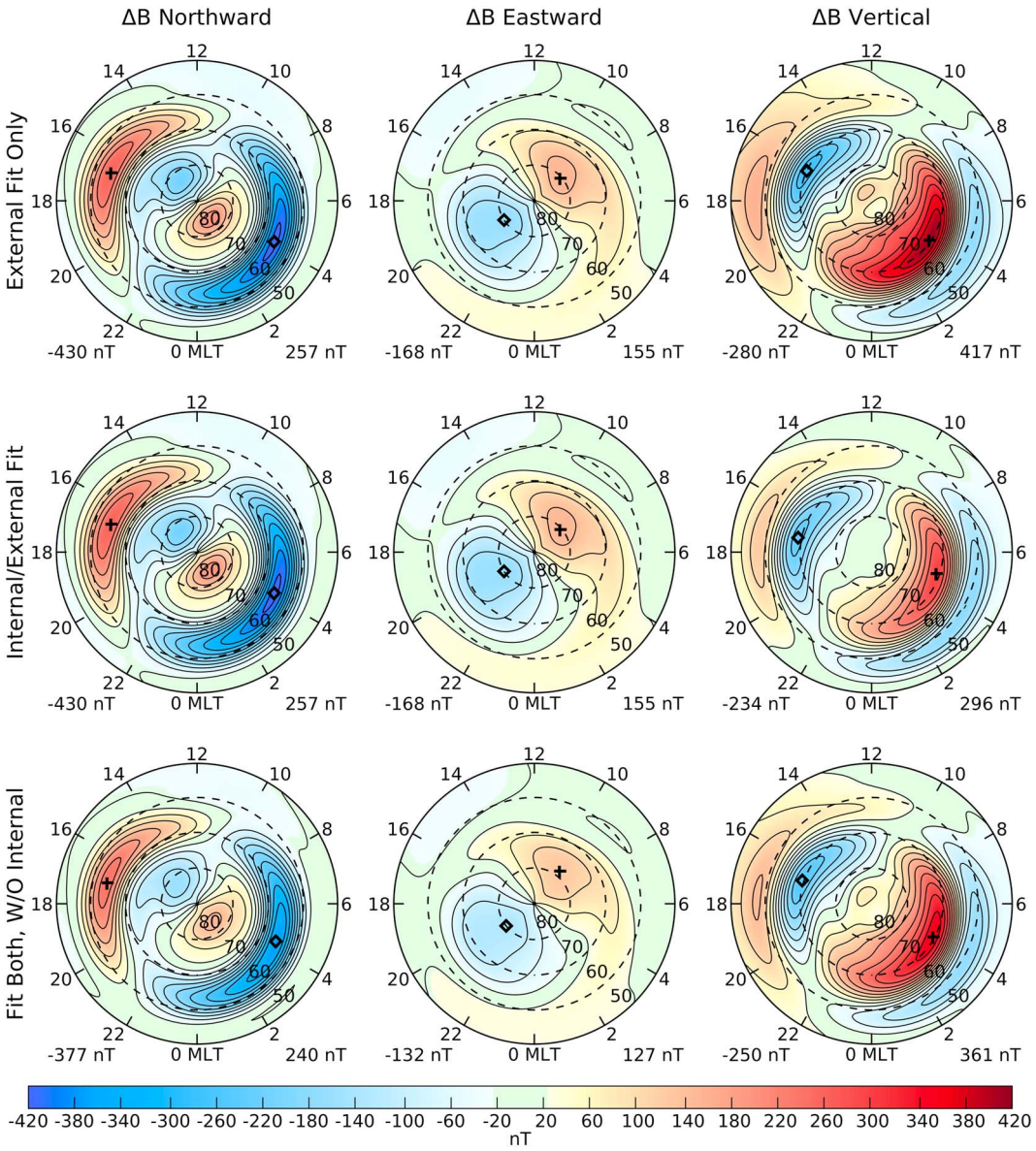

Figure 2. Example magnetic field values that are recalculated from the magnetic potential function after fitting the simulated data shown in Figure 1, through equations (1)–(5). The top row shows the results if only the external current sources are considered, and only the northward and eastward components used in the fit. The middle row shows the results if the internal sources are included, requiring the use of the vertical component in the fit. The bottom row shows results from the same fit as in the middle, but then removing the internal sources in equations (3)–(5). MLT = magnetic local time.

The bottom row in Figure 2 shows the results if both the internal and external sources are used for the fitting, as in the middle row, but then the internal terms are ignored when the magnetic field components are recalculated from the potential. This result has the benefit of revealing the relative contributions to the magnetic perturbations due to the external and internal sources, illustrating how the horizontal fields are reinforced by the telluric currents, while the vertical component is suppressed. In going from the bottom to middle row in this example, the strongest (negative) perturbation in the northward direction is increased by 14% by the internal current, and the magnitude of the eastward component increased by 27%, while the vertical component was reduced by 18%. The process was repeated for IMF clock angle orientations of 90°, 180°, and 270°, and IMF magnitudes of 5 and 10 nT. Looking at the changes in the magnitudes of both the positive and negative peaks in each component, it was found that the northward component had magnitude

increases in the range of 2% to 17%, the eastward component increased in magnitude by 7% to 28%, and the vertical component had magnitude decreases in the range of 1% to 19%.

3. Derivation of the Ionospheric Current Function

After the coefficients that define the magnetic potential function are determined, then the ionospheric (external) current function can be calculated. The origins of this methodology date back to earlier work by Chapman and Bartels (1940). As shown by Haines and Torta (1994), the formula is

$$\psi_E(\theta,\lambda) = \frac{a}{\mu_o}\sum_{k=1}^{K_e}\sum_{m=0}^{k}\frac{2k+1}{k+1}\left(\frac{R_2}{a}\right)^k P_k^m(\cos\theta)(g_k^{m,e}\cos m\lambda + h_k^{m,e}\sin m\lambda), \tag{6}$$

where R_2 is the radius of the spherical shell on which the external currents are assumed to flow, and a, as before, is the radius of the Earth. This function ψ_E has units of Amperes (or kA), and the current density vector is obtained from the negative gradient of this function, rotated by 90°. This current is referred to as the "equivalent current."

This "fictitious" overhead current must be divergence free (Richmond, 1995), and it is primarily related to ionospheric Hall currents. Pedersen currents may be included where the magnetic field overhead is not exactly vertical, and there are gradients in the conductivity (Fukushima, 1976, 1991). As mentioned by Fukushima (1991), the magnetic effects produced by three-dimensional currents in the space surrounding the Earth, including both the ionosphere and magnetosphere, can be reproduced by a two-dimensional, equivalent horizontal current. Any altitude can be chosen for this representation, with the solution being unique for a given altitude. The reverse is not true, as there is no unique configuration of three-dimensional currents that can be derived from a specified equivalent current.

Figure 3 shows examples of the current functions derived from the magnetic fields shown in Figure 1. The current function shown on the left side in part (a) is from the same fit shown in the top row of Figure 2, where only the external current sources are used, and not including the vertical component of the magnetic field. The middle part (b) shows the results from including both the external and internal sources, corresponding to the middle row in Figure 2. (The rightmost part (c) will be discussed later on.) In all cases, the value of the radius, R_2, is set to the radius of the Earth plus an altitude of 110 km. The equivalent current flows along the contour lines, while the total current flowing between contour lines is given by the difference between the contour levels, 50 kA in this example. The current density is higher where the contour lines are closer together. A comparison between (a) and (b) indicates that substantial differences result from not including the internal sources. The solution that did not include the effects of the internal sources had overestimated the ionospheric current by 18%. Any value greater than a can be used for R_2, and it does not need to be known when (1) is solved.

An arbitrary constant may be added to the current function, while maintaining the same derivatives. In these examples constants have been added so that the most positive and negative locations have the same absolute values. This optional level matching is done after the current function is calculated.

In these graphs the direction of the current flow is clockwise around a maximum, and counterclockwise around a minimum, following the same convention used by Kamide et al. (1981) and Richmond and Kamide (1988). For example, on the equatorward side of the maximum between 3 and 4 MLT the current is flowing westward. Others, including Haines and Torta (1994), favor the convention having the opposite sense, current flowing counterclockwise around the maximum, with the current function in (6) multiplied by −1.

For completeness, the equivalent current function for the internal sources is calculated from

$$\psi_I(\theta,\lambda) = -\frac{a}{\mu_o}\sum_{k=1}^{K_i}\sum_{m=0}^{k}\frac{2k+1}{k}\left(\frac{a}{R_1}\right)^{k+1} P_k^m(\cos\theta)(g_k^{m,i}\cos m\lambda + h_k^{m,i}\sin m\lambda), \tag{7}$$

where R_1 is the assumed radius of these internal currents. To be consistent with (6), equation (7) also uses a sign different from that shown by Haines and Torta (1994). The depth of the internal current is not well known and may have regional variations.

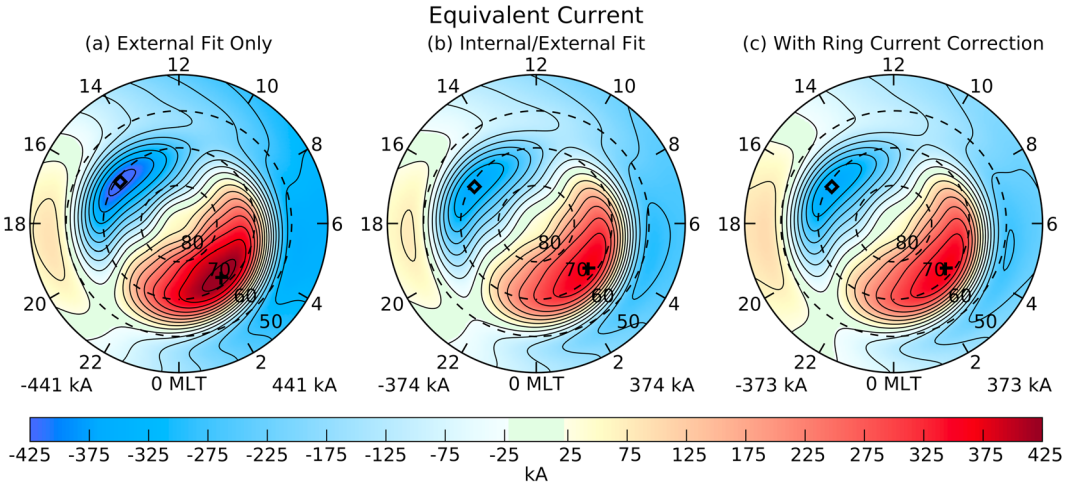

Figure 3. Example ionospheric current functions at an altitude of 110 km. These are derived with equation (6), using the simulated data shown in Figure 1. The graph in (a) is from the fitting that used only the external current sources, while (b) shows the results from fitting both the internal and external sources. (c) shows the same results after compensating for the effects of nonionospheric currents. MLT = magnetic local time.

4. Compensating for Currents Outside of the Ionosphere

While both the original data (Figure 1) and the equivalent current solution extend down to the magnetic equator, the illustrations in Figures 2 and 3 had shown only regions poleward of 50°, in order to better illustrate the high-latitude currents. In Figure 4 a the current function over the entire latitude range is shown, for the same solution already shown in Figure 3b. This pattern does not seem to be quite right, having too much current flowing at low latitudes. The reason for this is because the external sources include the ring current that flows around the Earth in the magnetosphere/radiation belts; this ring current appears here as if it were flowing in the ionosphere. Returning to Figure 1, it is seen that the empirical model includes the effects of this ring current, manifested as the negative values of the northward component at the equator, mostly on the dusk and night side (Weimer, 2013). In practice, these negative perturbations are indicated by the D_{st} index.

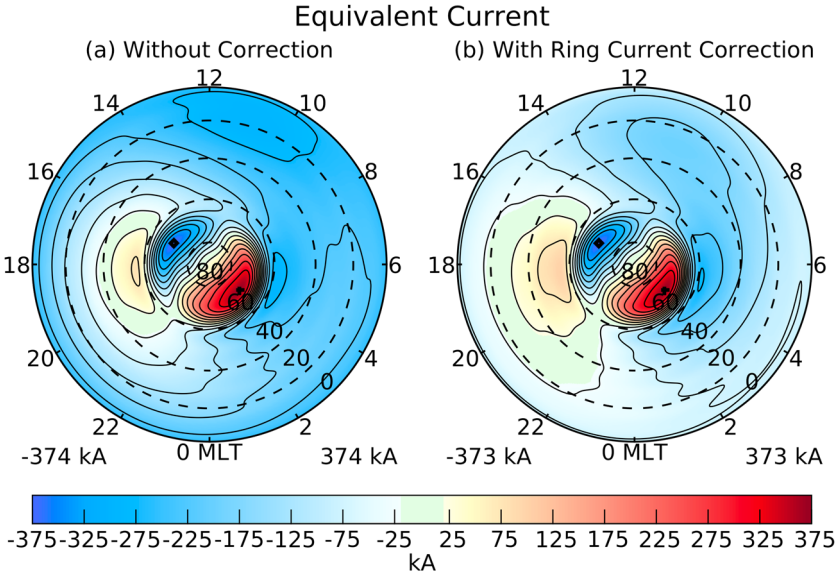

Figure 4. Example ionospheric current functions, over a wider range of latitudes. These are derived with equation (6), using the simulated data shown in Figure 1. The graph in (a) shows the same current function as Figure 3b, except extended to the equator. (b) shows the same results after compensating for the effects of nonionospheric currents, the same as Figure 3c.

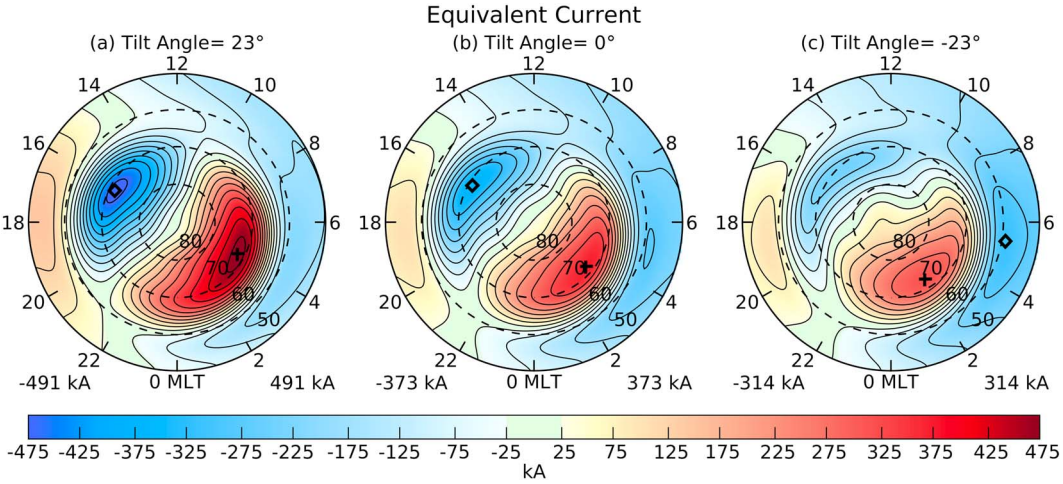

Figure 5. Example ionospheric current functions for different dipole tilt angles. All three use results from the empirical model for a 10-nT-southward interplanetary magnetic field and 400 km/s solar wind velocity. (a) The dipole tilt angle is +23°, corresponding to summer conditions. (b) The dipole tilt angle is 0°, corresponding to equinox. (c) The dipole tilt angle is −23°, corresponding to winter conditions. MLT = magnetic local time.

The magnetic influence of the ring current should be removed in order to get an accurate indication of the actual ionospheric currents, particularly as lower latitudes. As a very rough approximation, the magnitude of the ring current's perturbation magnetic field is obtained from the empirical model's output, using the mean value of the northward component at 0° latitude, from 18 to 2 MLT (through midnight). Using this value, a uniform field that is parallel to the Earth's magnetic axis was subtracted from the model's northward and vertical components. This solenoidal correction varied from entirely vertical at the pole, to northward (positive) at the equator. Figures 3c and 4b show the results from a recalculation of the equivalent current after this correction was made, with the result that the azimuthal currents at low latitudes have been significantly reduced. Other formulations for this correction were tried, but with less satisfactory results. Ultimately, it could be possible to develop a more accurate calculation of this correction, dealing with partial, asymmetrical ring currents, for example, that is beyond the scope of this report. The use of numerical, coupled magnetosphere-ring current models may be required.

Following the removal of the ring current disturbance, the revised currents at low latitudes show evidence of the "solar quiet" variations. For example, in the review by Matsushita (1975) his Figure 1A shows a map of the *Sq*° current in which the counterclockwise flow has a peak just below 30° latitude between 10 and 11 local time, with a changeover to a clockwise flow starting between 14 and 15 local time. Figure 4b has similar features, but since this map is for a disturbed time period (10 nT IMF) the quiet time *Sq*° features are not as prominent.

The reversed circulation cells just equatorward of 60° latitude near 6 and 18 MLT are not expected. One possibility is that these features could be due to the influence the upward and downward region 2 currents and their associated Pedersen currents; the conditions that are needed for these currents to produce no ground-level magnetic signature (radial orientation and no conductivity gradients; Fukushima, 1976) may not be valid here.

5. Example Ionospheric Currents for Other Conditions

The empirical model (Weimer, 2013) can generate magnetic perturbation fields for a wide range of conditions. It is useful to use this capability to explore how the equivalent currents change as well. One example showing the effects of tilt angle (seasonal) variations is shown in Figure 5. Not surprisingly, the summer case with +23° tilt angle in (a) has larger currents, due to more solar ionization and higher conductivities, compared to zero tilt in (b). For purpose of easy comparison, the IMF and solar wind velocity are the same as the prior examples. The currents are reduced even more when the dipole tilt angle is −23°, corresponding to winter conditions. The entire pattern rotates more clockwise, the dawn cell grows in size relative to dusk cell, and there are distortions near the center, due to the effects of the terminator. These results are similar

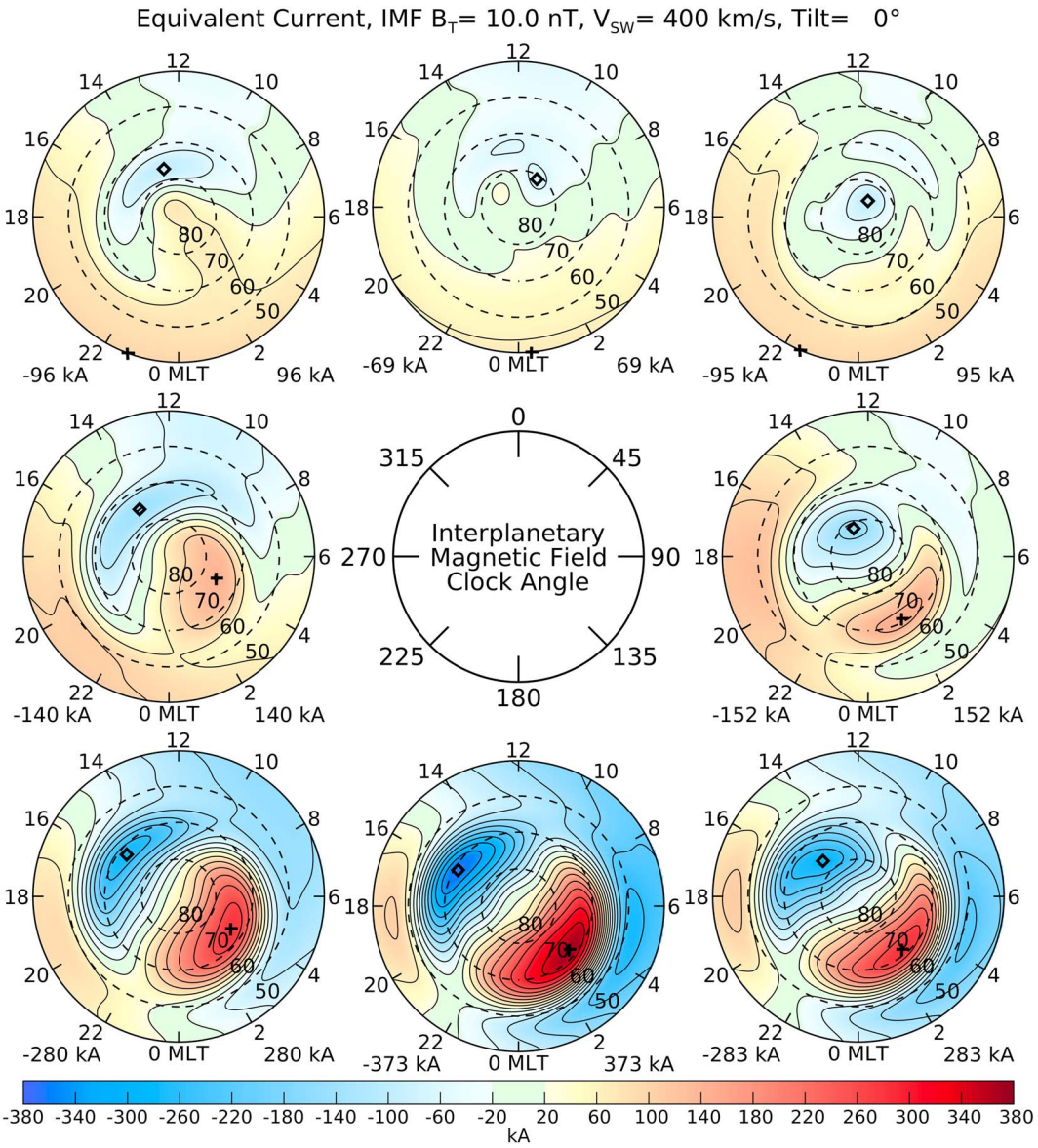

Figure 6. Example ionospheric current functions for different IMF clock angles. All three use results from the empirical model for an IMF with a magnitude of 10 nT, 400 km/s solar wind velocity, and zero dipole tilt. The IMF clock angle for the eight graphs are indicated in the center circle. IMF = interplanetary magnetic field; MLT = magnetic local time.

to those reported by Laundal, Gjerloev, et al.,(2016) and are consistent with the maps of rotated magnetic perturbation vectors shown by Friis-Christensen and Wilhjelm (1975) for the different seasons.

Figure 6 presents examples of the currents for eight different orientations of the IMF in the Geocentric Solar Magnetic *Y*-*Z* plane. The parameters are again the same as before, 10-nT IMF magnitude, 400 km/s solar wind velocity, and zero dipole tilt, so at 180° clock angle the pattern is familiar. Of particular interest is how the currents evolve between the clock angles 270° ($-Y$), 0° ($+Z$), and 90° ($+Y$). The resemblance of these equivalent currents to the corresponding electric potentials/convection patterns is impressive, even though entirely different types of measurements are used (Haaland et al., 2007; Ruohoniemi & Greenwald, 1996; Weimer, 1995), ranging from satellite probes to radars. Very similar results for the equivalent currents have also been shown by Friis-Christensen et al. (1985).

6. Discussion and Summary

The method shown here for calculation of the ionospheric equivalent current dates back to the derivations shown by Chapman and Bartels (1940), in sections 17.13 to 17.18. At first glance the equations do not appear similar, as Chapman and Bartels (1940) employ a shorthand notation for the summations, use different symbols, and also use Gaussian units rather than the International System units now preferred.

Chapman and Bartels (1940) also present another interesting application of these formulas, in which (1) can be reversed, so that if the spherical harmonic representation of the ionospheric current function is known, then the magnetic potential function at ground level can be derived. If the variables c and d represent the spherical harmonic coefficients for the external, current function in the ionosphere at radius R_2, in units of Amperes, then the magnetic potential at radii less than R_2 is

$$V(r,\theta,\lambda) = \mu_o \sum_{k=1}^{K_e} \sum_{m=0}^{k} \frac{k+1}{2k+1} \left(\frac{r}{R_2}\right)^k P_k^m(\cos\theta)(c_k^m \cos m\lambda + d_k^m \sin m\lambda). \tag{8}$$

One drawback of this reverse operation is that it does not include the contributions from the internal, telluric currents; it is possible to solve for an estimate of the telluric currents by finding the coefficients that, when combined with the external currents, produce a vertical magnetic field component that is zero at some depth, such as 400 km below the surface (Haines & Torta, 1994).

As mentioned earlier, modified apex coordinates have been used in the results shown here. It is noted that Laundal, Gjerloev, et al., (2016) and Laundal et al. (2018) prefer the "apex quasi-dipole" coordinate system, which is very similar, with identical mappings in longitude and MLT. Both coordinate systems are described by Laundal and Richmond (2017), which contains very good explanations of other coordinate systems commonly used in space science.

The spatial resolution of the spherical harmonic techniques is limited by the sparse distribution of magnetometers, particularly in oceans, if a solution is required for one point in time on a global scale, rather than average conditions. An alternative is to use a smaller, spherical cap that can be positioned over the region of interest (Haines & Torta, 1994). Other methods exist for deriving the ionospheric currents from ground-level magnetic field measurement, which are useful for smaller regions that have good coverage by an array of magnetometers. The list includes the "method of characteristics" (Amm, 1995, 2002), the "elementary current systems" or "elemental current method" (Amm, 1997, 2001), and the method of "spherical elementary currents (Amm & Viljanen, 1999; Pulkkinen et al., 2003; Weygand et al., 2011). Some applications are described by Amm et al. (2008), and Pulkkinen et al. (2003) demonstrate the separation of measured magnetic fields into both external and internal parts with the spherical elementary current system method.

The results shown here contain three items of significance. The first is that the internal currents were shown to enhance the horizontal magnetic fields at the surface by as much as 28% and reduce the vertical component by as much as 19%. While the amplification of the horizontal disturbance has been known for quite some time (i.e., Tanskanen et al., 2001), it is important to keep this in mind. For example, consider the case of using a numerical "first-principle" code to calculate the ionospheric currents and, from that, the surface magnetic field perturbations. If the internal current sources are not considered, then the horizontal fields that are derived may be too low. Similarly, a simulation may seem to have the correct result for the horizontal field values, but when the vertical field is examined then it could be found to be way too large, indicating that the results were obtained without the enhancing and reducing effects of the internal sources.

The second point is that solving for the magnetic potential function should include the internal, telluric sources, if the intent is to derive the ionospheric currents. Otherwise, the magnitudes of the equivalent current function will be overestimated, by approximately 20%.

Finally, for the greatest accuracy it is best to compensate for the magnetic field from the ring current when deriving the ionospheric current function; otherwise, the ring current is mapped into the ionosphere. While the effects of the ring current at high latitudes are subtle, at lower latitudes it become more important.

Appendix A: Computing the Least Squares Fits

The value of the magnetic potential function in equation (1) is established by the coefficients g_k^m and h_k^m, for both the internal and external sources. These coefficients are related to the northward, eastward, and vertical components of the measured magnetic field by (3)–(5). To solve for the coefficients from a given set of measurements by means of a least squares fit, the method of "LU decomposition" (Press et al., 1986, 1994) can be used. When reporting results in scientific journals, often the procedure name is simply stated and left at that. More specific details are provided in this appendix to make it easier for others, students in particular, to reproduce the results.

Assume that we have a set of N data points z_i of the quantity that is to be fit, where z_i are the measurements of a scalar potential or one component of a vector field component. $\bar{\mathbf{c}}$ is the set of unknowns to be obtained from the fit, the harmonic coefficients, and $\bar{\mathbf{r}}_\mathbf{i}$ is a set of N position or state vectors corresponding to each point z_i. The function that is fit, $f(\bar{\mathbf{r}})$ is evaluated for each coefficient, so it has the same number of elements as $\bar{\mathbf{c}}$ times N. This function evaluation will be referred to as $\bar{\mathbf{x}}_i$ here.

If $\bar{\mathbf{c}}$ were to have only three elements, then

$$\bar{\mathbf{x}}_i \cdot \bar{\mathbf{c}} = x_{0i}c_0 + x_{1i}c_1 + x_{2i}c_2 \tag{A1}$$

for the ith of N points. This result is easy to generalize to a larger, arbitrary number of parameters. The square of the error is defined as

$$\sigma^2 = \sum_i^N \left(z_i - \bar{\mathbf{x}}_i \cdot \bar{\mathbf{c}}\right)^2. \tag{A2}$$

Substituting (1) into (2), the square error is expanded to

$$\sigma^2 = \sum_i^N \left(z_i - x_{0i}c_0 - x_{1i}c_1 - x_{2i}c_2\right)^2. \tag{A3}$$

The lowest square error is found where the derivative of σ^2 with respect to each term in the series is zero. For example,

$$\frac{\partial(\sigma^2)}{\partial c_0} = -2\sum_i^N x_{0i}\left(z_i - x_{0i}c_0 - x_{1i}c_1 - x_{2i}c_2\right) = 0, \tag{A4}$$

leading to

$$c_0\sum_i^N x_{0i}x_{0i} + c_1\sum_i^N x_{0i}x_{1i} + c_2\sum_i^N x_{0i}x_{2i} = \sum_i^N z_i x_{0i}, \tag{A5}$$

likewise for $c_1 c_2$ and

$$c_0\sum_i^N x_{1i}x_{0i} + c_1\sum_i^N x_{1i}x_{1i} + c_2\sum_i^N x_{1i}x_{2i} = \sum_i^N z_i x_{1i}, \tag{A6}$$

$$c_0\sum_i^N x_{2i}x_{0i} + c_1\sum_i^N x_{2i}x_{1i} + c_2\sum_i^N x_{2i}x_{2i} = \sum_i^N z_i x_{2i}. \tag{A7}$$

These three equations can be written in matrix form as

$$\mathbf{A} \cdot \mathbf{c} = \mathbf{b}, \tag{A8}$$

where both $\mathbf{A}$ and $\mathbf{b}$ are known and a solution is needed for $\mathbf{c}$. The elements of $\mathbf{b}$, a three-element column vector in this example, are obtained from

$$b_j = \sum_i^N z_i x_{ji}, \tag{A9}$$

and the elements of **A**, a 3 × 3 matrix, are obtained from

$$A_{jk} = \sum_{i}^{N} x_{ji} x_{ki}. \tag{A10}$$

If there are M elements in **c**, then **b** has M elements, and **A** is a $M \times M$ matrix. In equations (1)–(5), the g_k^m and h_k^m correspond to the coefficients in $\bar{\mathbf{c}}$, and the $P_k^m(\cos\theta)\cos m\lambda$ and $P_k^m(\cos\theta)\sin m\lambda$ terms (or their derivatives) correspond to the $\bar{\mathbf{x}}_i$ computed for each coefficient at all of the N points. In the IDL programming language, the solution for **c** can be obtained by use of the function **LUSOL** with arrays **A** and **b**, after first preconditioning **A** with the **LUDC** procedure.

Programmers could be inclined to put all coefficients into a three-dimensional array that has dimensions [Max k,Max m,2], but since $m \leq k$ and only odd $k - m$ terms are used, many array elements would not be used. To simplify some aspects of the coding and storage efficiency, it is better to compress the coefficients g_k^m and h_k^m into a one-dimensional array with the number of elements M. Three other arrays of the same size M are needed to hold the corresponding values of l, m, and a flag that indicates with a 0 or 1 whether the $g\cos m\lambda$ or $h\sin m\lambda$ term is contained. If both "external" and "internal" sources are fit, then the M that indicates the size of the matrices **A** and **b** is doubled. In the examples that were shown in the figures, the maximum value of k was 34 and m values up to 3 were used, with the result that $M = 115$ (using only odd $k - m$ terms). So the array A is often quite large.

It is useful to know that if two or more different functions, such as components of a vector, are being fit with identical data locations but different values of z_i, then the **A** matrix and the result from **LUDC** only needs to be calculated once. Only the **b** array and the result from the **LUSOL** function need to be recalculated for each component.

A similar method can be used to derive an empirical model, in which each of the g_k^m and h_k^m are also fit to a number of input parameters, such as solar wind and IMF values, in addition to the locations. For example, in the model described by Weimer (2013), each of three vector components are described by 108 spherical harmonic coefficients that are controlled by 17 input parameters, and the matrix A used in the solution had 3,060 × 3,060 elements. Furthermore, the input data were from approximately 130 magnetometers, taken at 1-min intervals over an 8-year period (more than $5 \cdot 10^8$ points), and the calculation of these arrays can run into days. In this case the calculation of the **A** and **b** matrices can be split among different processing jobs, which do not even need to be done on the same computer. Each job is assigned a fraction of the N data points, and after they finish, then the matrix elements only need to be added together before calling **LUDC**. If a language such as IDL is used, then most of the computing time can be spent with just the calculation of the matrix **A**, so it is worthwhile to pass this task off to a subroutine that uses a compiled language, such as FORTRAN.

Acknowledgments
This work is supported by the National Science Foundation Grant AGS-1638270 to Virginia Tech, with additional support from a subcontract to Hampton University, on NASA Grant NNX15AE05G. An archive of the magnetic perturbation map data that were used to generate all example figures plus the spherical harmonic coefficients that were calculated and IDL code are available online (https://doi.org/10.5281/zenodo.2538170).

References

Amm, O. (1995). Direct determination of the local ionospheric Hall conductance distribution from two-dimensionalelectric and magnetic field data: Application of the method using models of typical ionospheric electrodynamic situations. *Journal of Geophysical Research*, *100*(A11), 21,473–21,488. https://doi.org/10.1029/95JA02213

Amm, O. (1997). Ionospheric elementary current systems in spherical coordinates and their application. *Journal of Geomagnetism and Geoelectricity*, *49*(7), 947–955. https://doi.org/10.5636/jgg.49.947

Amm, O. (2001). The elementary current method for calculating ionospheric current systems from multisatellite and ground magnetometer data. *Journal of Geophysical Research*, *106*(A11), 24,843–24,856. https://doi.org/10.1029/2001JA900021

Amm, O. (2002). Method of characteristics for calculating ionospheric electrodynamics from multisatellite and ground-based radar data. *Journal of Geophysical Research*, *107*(A10), SMP 3–1-SMP 3-12. https://doi.org/10.1029/2001JA005077

Amm, O., Aruliah, A., Buchert, S. C., Fujii, R., Gjerloev, J. W., Ieda, A., & Yoshikawa, A. (2008). Towards understanding the electrodynamics of the 3-dimensional high-latitude ionosphere: Present and future. *Annales Geophysicae*, *26*, 3913–3932. https://doi.org/10.5194/angeo-26-3913-2008

Amm, O., & Viljanen, A. (1999). Ionospheric disturbance magnetic field continuation from the ground to the ionosphere using spherical elementary currents systems. *Earth Planets Space*, *51*, 431–440. https://doi.org/10.1186/BF03352247

Chapman, S., & Bartels, J. (1940). Geomagnetism, *Analysis of the data, and physical theories* (Vol. II, 1049 pp.). London: Oxford University Press.

Emmert, J. T., Richmond, A. D., & Drob, D. P. (2010). A computationally compact representation of magnetic-apex and quasi-dipole coordinates with smooth base vectors. *Journal of Geophysical Research*, *115*, A08322. https://doi.org/10.1029/2010JA015326

Friis-Christensen, E., Kamide, Y., Richmond, A. D., & Matsushita, S. (1985). Interplanetary magnetic field control of high-latitude electric fields and currents determined from Greenland magnetometer data. *Journal of Geophysical Research*, *90*, 1325. https://doi.org/10.1029/JA090iA02p01325

Friis-Christensen, E., & Wilhjelm, J. (1975). Polar cap currents for different directions of the interplanetary magnetic field in the YZ plane. *Journal of Geophysical Research*, *80*(10), 1248–1260. https://doi.org/10.1029/JA080i010p01248

Fukushima, N. (1976). Generalized theorem for no ground magnetic effect of vertical currents connected with Pedersen currents in the uniform conducting ionosphere. *Report of Ionosphere and Space Research in Japan*, *30*(1-2), 35–40.

Fukushima, N. (1991). Field-aligned currents in the magnetosphere. *Geofisica Internacional*, *30*(4), 241–248.

Gjerloev, J. W. (2012). The Super MAG data processing technique. *Journal of Geophysical Research*, *117*, A09213. https://doi.org/10.1029/2012JA017683

Green, D. L., Waters, C. L., Korth, H., Anderson, B. J., Ridley, A. J., & Barnes, R. J. (2007). Technique: Large-scale ionospheric conductance estimated from combined satellite and ground-based electromagnetic data. *Journal of Geophysical Research*, *112*, A05303. https://doi.org/10.1029/2006JA012069

Haaland, S. E., Paschmann, G., Forster, M., Quinn, J. M., Torbert, R. B., McIlwain, C. E., et al. (2007). High-latitude plasma convection from Cluster EDI measurements: Method and IMF-dependence. *Annales Geophysicae*, *25*, 239–253.

Haines, G. V. (1985). Spherical cap harmonic analysis. *Journal of Geophysical Research*, *90*(B3), 2583. https://doi.org/10.1029/JB090iB03p02583

Haines, G. (1988). Computer programs for spherical cap harmonic analysis of potential and general fields. *Computers and Geosciences*, *14*(4), 413–447. https://doi.org/10.1016/0098-3004(88)90027-1

Haines, G. V., & Torta, J. M. (1994). Determination of equivalent current sources from spherical cap harmonic models of geomagnetic field variations. *Geophysical Journal International*, *118*(3), 499–514. https://doi.org/10.1111/j.1365-246X.1994.tb03981.x

Hapgood, M. A. (1992). Space physics coordinate transformations: A user guide. *Planetary and Space Science*, *40*(5), 711–717.

Hapgood, M. A. (1997). Corrigendum. *Planetary and Space Science*, *45*(8), 1047.

Kamide, Y., Richmond, A. D, & Matsushita, S. (1981). Estimation of ionospheric electric fields, ionospheric currents, and field-aligned currents from ground magnetic records. *Journal of Geophysical Research*, *86*(A2), 801–813. https://doi.org/10.1029/JA086iA02p00801

Laundal, K. M., Finlay, C. C., & Olsen, N. (2016). Sunlight effects on the 3D polar current system determined from low Earth orbit measurements. *Earth, Planets and Space*, *68*, 142. https://doi.org/10.1186/s40623-016-0518-x

Laundal, K. M., Finlay, C. C., Olsen, N., & Reistad, J. P. (2018). Solar wind and seasonal influence on ionospheric currents from Swarm and CHAMP measurements. *Journal of Geophysical Research: Space Physics*, *123*, 4402–4429. https://doi.org/10.1029/2018JA025387

Laundal, K. M., Gjerloev, J. W., Ostgaard, N., Reistad, J. P., Haaland, S., Snekvik, K., & Milan, S. E. (2016). The impact of sunlight on high-latitude equivalent currents. *Journal of Geophysical Research: Space Physics*, *121*, 2715–2726. https://doi.org/10.1002/2015JA022236

Laundal, K. M., & Richmond, A. D. (2017). Magnetic coordinate systems. *Space Science Reviews*, *206*, 27–59. https://doi.org/10.1007/s11214-016-0275-y

Matsushita, S. (1975). Morphology of slowly-varying geomagnetic external fields—A review. *Physics of the Earth and Planetary Interiors*, *10*, 299–312. https://doi.org/10.1016/0031-9201(75)90056-4

Pothier, N. M., Weimer, D. R., & Moore, W. (2015). Quantitative maps of geomagnetic perturbation vectors during substorm onset and recovery. *Journal of Geophysical Research: Space Physics*, *120*, 1197–1214. https://doi.org/10.1002/2014JA020602

Press, W. H., Flannery, B. P., Teukolsky, S. A., & Vetterling, W. T. (1986). *Numerical recipes: The art of scientific computing*. New York: Cambridge University Press.

Press, W. H., Teukolsky, S. A., Vetterling, W. T., & Flannery, B. P. (1994). *Numerical recipes in C: The art of scientific computing, second edition* (2nd ed.). New York: Cambridge University Press.

Pulkkinen, A., Amm, O., & Viljanen, A. (2003). Ionospheric equivalent current distributions determined with the method of spherical elementary current systems. *Journal of Geophysical Research*, *108*(A2), 1053. https://doi.org/10.1029/2001JA005085

Pulkkinen, A., Amm, O., Viljanen, A., & BEAR working group (2003). Separation of the geomagnetic variation field on the ground into external and internal parts using the spherical elementary current system method. *Earth Planets Space*, *55*, 117–129. https://doi.org/10.1186/BF03351739

Richmond, A. D. (1995). Ionospheric electrodynamics using magnetic apex coordinates. *Journal of Geomagnetism and Geoelectricity*, *47*, 191. https://doi.org/10.5636/jgg.47.191

Richmond, A. D., & Kamide, Y. (1988). Mapping electrodynamic features of the high-latitude ionosphere from localized observations: Technique. *Journal of Geophysical Research*, *93*(A6), 5741–5759. https://doi.org/10.1029/JA093iA06p05741

Ruohoniemi, J. M., & Greenwald, R. A. (1996). Statistical patterns of high-latitude convection obtained from Goose Bay HF radar observations. *Journal of Geophysical Research*, *101*, 21,743–21,763. https://doi.org/10.1029/96JA01584

Tanskanen, E. I., Viljanen, A., Pulkkinen, T. I., Pirjola, R., Häkkinen, L., Pulkkinen, A., & Amm, O. (2001). At substorm onset, 40% of AL comes from underground. *Journal of Geophysical Research*, *106*(A7), 13,119–13,134. https://doi.org/10.1029/2000JA900135

VanZandt, T. E., Clark, W. L., & Warnock, J. M. (1972). Magnetic apex coordinates: A magnetic coordinate system for the ionospheric F_2 layer. *Journal of Geophysical Research*, *77*, 2406. https://doi.org/10.1029/JA077i013p02406

Weimer, D. (1995). Models of high-latitude electric potentials derived with a least error fit of spherical harmonic coefficients. *Journal of Geophysical Research*, *100*, 19,595. https://doi.org/10.1029/95JA01755

Weimer, D. R. (2013). An empirical model of ground-level geomagnetic perturbations. *Space Weather*, *11*, 107–120. https://doi.org/10.1002/swe.20030

Weimer, D. R., Clauer, C. R., Engebretson, M. J., Hansen, T. L., Gleisner, H., Mann, I., & Yumoto, K. (2010). Statistical maps of geomagnetic perturbations as a function of the interplanetary magnetic field. *Journal of Geophysical Research*, *115*, A10320. https://doi.org/10.1029/2010JA015540

Weygand, J. M., Amm, O., Viljanen, A., Angelopoulos, V., Murr, D., Engebretson, M. J., & Mann, I. (2011). Application and validation of the spherical elementary currents systems technique for deriving ionospheric equivalent currents with the North American and Greenland ground magnetometer arrays. *Journal of Geophysical Research*, *116*, A03305. https://doi.org/10.1029/2010JA016177